Neutrosophic Sets and Systems, Vol. 68, 2024
University of New Mexico

Assessment of deep learning techniques for bone fracture detection under neutrosophic domain

Doaa El-Shahat[1*], Ahmed Tolba[1]

[1]Faculty of Computers and Informatics, Zagazig University, Shaibet a Nakareyah, Zagazig, Ash Sharqia Governorate, 44519, Egypt, doaazidan@zu.edu.eg; a.tolba24@fci.zu.edu.eg;

***Correspondence: doaazidan@zu.edu.eg**

Abstract

With the increasing strain on the health system, there is a growing need for automatic medical image diagnosis. Emerging technologies for medical diagnosis can help to achieve the goals of sustainable development. However, analyzing medical images can be challenging due to uncertain data, ambiguity, and impreciseness. To address this issue, we have developed a novel BoneNet-NS technique to classify fractures in X-ray bone images. The proposed approach is based on the power of deep learning (DL) and neutrosophic set (NS) to deal with aleatoric uncertainty. Moreover, we present two frameworks for integrating NS with DL models: BoneNet-NS1 and BoneNet-NS2. We employ various DL models, including Xception, ResNet52V2, DenseNet121, and customized CNN to evaluate both frameworks. Furthermore, 4924 X-ray bone images are utilized to distinguish between fractured and non-fractured classes. The statistical analyses demonstrate that BoneNet-NS2 performs better than BoneNet-NS1 for most DL models. Specifically, using the ResNet52V2 model, our proposed BoneNet-NS2 achieved the highest accuracy, log loss, precision, recall, F1-score, and AUC with values of 99.7%, 0.006, 99.7%, 99.7%, 99.7%, and 99.7%, respectively.

Keywords: Deep Learning; Neutrosophic Set; Bone Fracture Detection; Artificial Intelligence

---

1. Introduction

Bone fractures and cracks usually result from exposure to falling, direct blows to the body, collisions, such as traffic accidents or bullet wounds, and injuries resulting from playing sports. These fractures are diagnosed through X-rays, which are considered one of the cheapest types of medical imaging modalities. Furthermore, X-rays can be used in mobile or wsearable devices for quick and accurate fracture detection, utilizing DL algorithms for diagnosis and detection [1]. X-ray images suffer some noise, fuzziness, vagueness, impreciseness, and uncertainty. These aleatoric uncertainties result in low-quality images, bad image contrast, and edge representation.

DL models performance can be affected by aleatoric uncertainty or data uncertainty. This sort of uncertainty is caused by intrinsic noise in the data, such as measurement error or imprecise annotation, which cannot be decreased by gathering more data [2].

Aleatoric uncertainty must be quantified and identified [3] to be eliminated using different techniques, including wavelet thresholding, Gaussian smoothing, and anisotropic filtering. However, these methods often result in losing some image details or creating unrealistic contrast, making it harder to identify diseases. There are numerous deblurring techniques, such as the Richardson-Lucy algorithm, Wiener filter, regularized filter, and inverse filter. These methods can lead to noise amplification, boundary artifacts, and high computational requirements. Similarly, contrast enhancement methods like normalization, histogram equalization, low and high pass, and contrast stretching, can result in abnormal brightness, unnatural appearance, and noise amplification [4].

Soft computing techniques address the widespread imprecision and ambiguity of real-world problems. Fuzzy set (FS) has been presented by Zadeh [5] to handle data uncertainty using membership degree. Many bone fracture classification studies used FS to deal with uncertainty. Vasilakakis et al. [6] introduced wavelet fuzzy phrases (WFP) for feature extraction and bone fracture diagnosis. It extracts textural information from 2D discrete wavelet transform (DWT) images using FS. The words create sentences that represent the image's contents. The approach obtains a classification accuracy of 84%, outperforming other cutting-edge methods.

Intuitionistic Fuzzy Set (IFS) was introduced in 1986 to handle uncertainty by associating each element to membership degree and non-membership degree. In this context, singh et al. [7] proposed a segmentation paradigm for brain MR images that takes into account noise, intensity inhomogeneity (IH), uncertainty, and structural complexity. The framework uses local spatial and gray level information as a local parameter-free fuzzy factor to maintain the quantity of structural features. It incorporates a novel method to IH and employs IFS theory to eliminate uncertainty in assigning membership to pixels near tissue borders. A process is devised to generate artifact-free pictures that may be compared to the original image for expert interpretation.

Soft computing approaches such as FS and IFS aim to handle the uncertainties within data, but they suffer from certain issues, such as [8]:

- In IFS, the sum of membership values is 1.
- IFS and FS can't differentiate between relative truth (truth in at least one world) and absolute truth (truth in all possible worlds).
- Elements in IFS can't be non-standard.
- IFS and FS can't deal with some contradiction paradoxes.

In 1998, Smarandache [8] introduced a neutrosophic set (NS) to deal with higher dimensions of uncertainty. NS can associate each element in the universe with three independent degrees of membership: true, indeterminacy, and false. The values of membership range from $]^{-}0, 1^{+}[$ in a non-standard unit interval. NS can deal with some contradictory paradoxes. But in image analysis and processing, many studies deal with interval [0,1] because deal with image intensities in range $]^{-}0, 1^{+}[$ is difficult [9].

DL methods show great results and performance in medical image classification. Can et al. [10] introduced an alternative pooling layer, named the common vector approach pooling approach, to solve the restrictions associated with average pooling in DL algorithms. The trials are carried out on a huge dataset containing twenty distinct dental diseases classified into seven groups. Our suggested technique achieved a high accuracy rate of 86.4% for recognizing dental issues across the seven oral categories. Wang et al. [11] proposed a novel intelligent defect diagnosis method based on hybrid DL for chip X-ray images. The system has four stages: image segmentation, normalization, reconstruction, defect identification, contour matching, and qualification diagnostics. The system's efficacy and resilience are tested on real-world inspection lines, with an evaluation accuracy of 92.5%.

In this study, we introduce an integrated framework between DL and NS to handle uncertainty in three degrees of membership for bone fracture classification. The two frameworks employ four different DL models, such as Xception, ResNet152V2, DenseNet121, and customized CNN in terms of accuracy, binary cross entropy loss/log loss, precision, recall, F1-score, and area under curve (AUC). Hence, the main contribution of this paper can be stated as follows:

- We apply the uncertainty handling feature to power DL models. The uncertainty was handled using three degrees of membership: true, indeterminacy, and falsity.
- Two different frameworks were proposed to combine DL with NS, and a comparison was made between them using four different DL models.
- The first framework (BoneNet-NS1) integrates an NS image (true image, indeterminacy image, false image) as input to the DL model.
- In the second framework (BoneNet-NS2), some enhancement on the NS image has been done, and then the NS image is converted to gray-scale images as input to the DL model.
- The proposed work was evaluated on a bone fracture dataset with 4924 images, classified into fractured and non-fractured images.
- The second framework (BoneNet-NS2) shows superior results compared to the first framework (BoneNet-NS1) for most DL models.
- ResNet52V2 shows the highest results using (BoneNet-NS2) in terms of accuracy, log loss, precision, recall, F1-score, and AUC with 99.7 %, 0.006, 99.7%, 99.7%, 99.7%, and 99.7, respectively.

The remainder of the paper is divided as follows. Section 2 provides the related work for this study. Section 3 presents the methodology for the NS and DL algorithms. Moreover, section 4 introduces the steps of the proposed approach. Section 5 presents experimental results. Section 6 provides the managerial Implications and section 7 illustrates the conclusions and future directions of our work.

2. Related work

In this section, we summarize some recent studies that integrate the DL with NS in the medical field. Khalifa et al. [12] investigated the influence of NS on DL models utilizing restricted COVID-19 x-ray datasets. The work used Alexnet, Googlenet, and Restnet18 DL models to transform medical images from grayscale to the NS domain, which includes True (T), Indeterminacy (I), and Falsity (F) images. Over 36 trials were completed, and the Indeterminacy (I) NS domain achieved the highest testing accuracy and performance metrics of 87.1%. Hu et al. [13] introduced the NeutSS-PLP technique for extracting polyp regions from colonoscopy images, which employs a short-connected saliency detection network with NS enhancement. The approach improves specular reflection identification in colonoscopy images by establishing local and global thresholds and defining T, I, and F functions. The approach also incorporates two-level short connections to make use of multi-level and multi-scale capabilities.

Cai et al. [14] proposed an automatic detection method for MCCs that employs NS domain transformation, similar to a standard CAD system. A DCNN1 classifier was developed to distinguish individual MCs while reducing FP MCs. A novel adaptive NRSL technique was used to accelerate the learning process. For cluster-based evaluation, the MCC detection technique achieved 92.5% sensitivity at 0.50 frames per second per image. A strong DCNN2 classifier was developed for diagnosis using automatic detection, with AUCs of 0.908 and 0.872, respectively. The results indicate that the suggested approach considerably enhances the automatic detection and classification of MCCs on FFDMs.

Yasser et al. [15, 16] introduced a reliable and intuitive diagnostic technique for automatically identifying COVID-19 using digital chest X-rays. The tool employs a hybrid architecture that combines NS approaches and ML. Classification characteristics are retrieved from X-ray images utilizing morphological features and PCA. The ML networks divide chest X-rays into positive COVID-19 patients and normal people. Guo and Ashour [17] presented a classification model consisting of two stages: multiple deep convolution neural networks (MDCNN) and NSS approach. The NMDCNN determines reinforced training numbers for each epoch using NSS and then classifies dermoscopic images as malignant or benign using incremental learning and maximum voting. The model's competence was evaluated using the International Skin Imaging Collaboration dataset.

Özyurt et al. [18] introduced the NS-EMFSE technique to classify tumor areas in brain imaging as benign or malignant. CNN characteristics were utilized to classify data, along with support vector machine (SVM) and KNN classifiers. An experimental study of 80 benign and 80 malignant tumors revealed outstanding classification performance with several classifiers, with CNN features outperforming SVM with an average success rate of 95.62%. Another contribution by Talouki et al. [19] presented a novel image completion approach that uses NS-based segmentation to fill in image holes. This strategy decreases spatial and intensity ambiguity, maintains boundaries and homogeneity, and minimizes discontinuity. The method favors outside pixels and employs extended similarity criteria to identify patches with the best match.

Guo et al. [20] presented a deep neural network (DNN) for WBC extraction from blood images, with an emphasis on object indeterminacy in the NS domain. The network uses WBC indeterminacy as a fusion component to enable segmentation into discrete areas. The model surpasses three original encoder-decoder networks, reaching high precision rates and the greatest mean segmentation accuracy (0.95301).

Table 1 summarizes all the aforementioned related works in terms of year, task, disease, modality, dataset, number of images, number of classes, model, and the obtained accuracy. From these studies, it was concluded that NS studies using DL are still growing. Also, there are no studies on bone fracture classification based on NS and DL. So, in our study, we proposed a novel approach that integrates the environment of NS and DL on X-ray images for bone fracture classification.

Table 1 Summary of previous works using NS and DL for medical image analysis

Ref.	Year	Task	Disease	Modality	Dataset	No. images	No.classes	Model	Accuracy
[12]	2021	Classification	COVID-19	X-ray	COVID-19 x-ray dataset	306	4	Alexnet, Googlenet, Restnet1	87.1% for I domain
[13]	2022	Segmentation	Colorectal polyp	-	EndoScene, Kvasir-SEG	EndoScene=912 Kvasir-SEG=1000	EndoScene =8 Kvasir-SEG =4	saliency detection network	EndoScene =0.971,
[14]	2019	Cluster, classification	Breast cancer	Mammograms	NFH dataset	676	2	DCNN	0.813
[15, 16]	2020,2022	Classification	Covid-19	X-ray	COVID-19 Dataset, healthy dataset	570	2	(MFs), (PCA)	98.46%
[17]	2019	classification	Skin cancer	dermoscopic images	c ISIC2016	1279	2	MDCNN	85.22%
[18]	2019	Segmentation, Classification	Brain tumor	MRI	TCIA	500	2	CNN	95.62%.
[19]	2024	image completion	-	-	-	-	-	-	-
[20]	2024	Segmentation	-	pathological imaging	three datasets	Varies	5	Encoder-Decoder	95.3%

3. Preliminaries

Definition 1: Neutrosophic set (NS)

In NS, The element X in the universe can be associated with three membership function $\{True\_Membership, Indeterminacy\_Membership, False\_Membership\}$ as {T, I, F} [21]. This independent membership values are ranging from zero and one, where $0 \leq T + I + F \leq 3$. The Standard and non-standard NS has interval$]^{-}0, 1^{+}[$. Many real studies utilize interval of $[0,1]$ instead of $]^{-}0, 1^{+}[$ as it is hard to use in some problems with exact values. The NS can handle indeterminacy value by introducing a 3-D of membership, as in Figure 1, in contrast of IFS that introduce only 2-D membership degrees. For each element X in NS, where X is continuous, the NS can be denoted as follows [22, 23]:

$$NS = \int_{\mathrm{X}} < T(\mathrm{x}), I(\mathrm{x}), F(\mathrm{x})/\mathrm{x}, \mathrm{x} \in \mathrm{X} > \tag{1}$$

Since X is discrete, the NS can be denoted as follows:

$$NS = \sum_{i=1}^{n} < T(\mathrm{x}_i), I(\mathrm{x}_i), F(\mathrm{x}_i)/\mathrm{x}_i, \mathrm{x}_i \in \mathrm{X} > \tag{2}$$

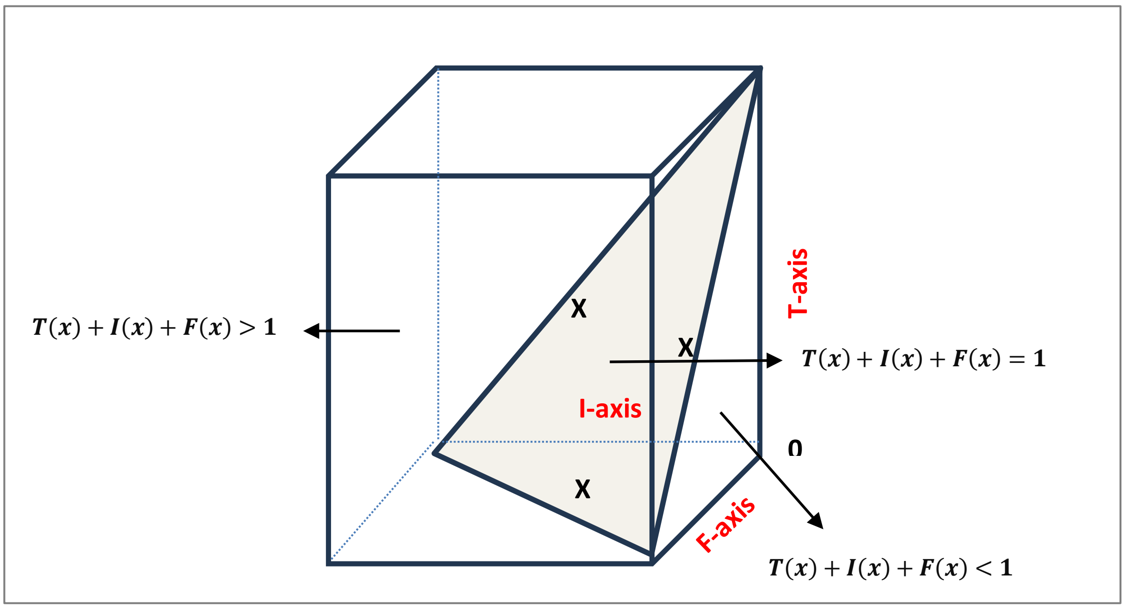

Figure 1 NS True, Indeterminacy, False membership functions [24].

Definition2: Image in NS domain

The pixel is denoted as (True, Indeterminacy, False) memberships, which can be represented as:

$$P_{NS}(a, b) = \{True(a, b), Indeterminacy(a, b), False(a, b)\} \tag{3}$$

The True, Indeterminacy, and False can be represented as follows:

$$True(x, \mathrm{y}) = \frac{\bar{g}(x, \mathrm{y}) - \bar{g}_{min}}{\bar{g}_{max} - \bar{g}_{min}} \tag{4}$$

$$\bar{g}(x,y) = \left(\frac{1}{window \times window}\right) \sum_{m=i-window/2}^{i+window/2} \sum_{n=j-window/2}^{j+window/2} g(m,n) \tag{5}$$

$$False(x,y) = 1 - True(x,y) \tag{6}$$

$$\delta(x,y) = abs(g(x,y) - \bar{g}(x,y)) \tag{7}$$

$$Indeterminacy(x,y) = \frac{\delta(x,y)-\delta_{min}}{\delta_{max}-\delta_{min}} \tag{8}$$

where $\bar{g}(x,y)$ is the local mean-value (LV) of the image, $\delta(x,y)$ is the absolute value (AV) define by the difference between intensity and LV [25].

Definition 3: NS Entropy

The entropy of an image reveals how the intensity is distributed. The high entropy value suggests that the pixel probability and uniform distribution are identical. In contrast, the minimal entropy value implies an inequality in pixel probability and a non-uniform distribution. The NS entropy is expressed as follows:

$$E_{NS} = E_{True} + E_{Indeterminacy} + E_{False} \tag{9}$$

$$E_{True} = -\sum_{i=min\{True\}}^{max\{True\}} p_{True}(i) ln P_{True}(i) \tag{10}$$

$$E_{Indeterminacy} = -\sum_{i=min\{Indeterminacy\}}^{max\{Indeterminacy\}} p_{IIndeterminacy}(i) ln P_{Indeterminacy}(i) \tag{11}$$

$$E_{False} = -\sum_{i=min\{False\}}^{max\{False\}} p_{False}(i) ln P_{False}(i) \tag{12}$$

Since E_{True} , $E_{Indeterminacy}$, and E_{False} are entropies for True, Indeterminacy, and False, respectively.

Definition 4. α-mean operation

This operation aims to minimize the IM by computing the mean value between the neighbors in NS image:

$$\bar{P}(\alpha) = Pixel(\overline{True}(\alpha), \overline{IIndetermınacy}(\alpha), \overline{False}(\alpha)) \tag{13}$$

$$\overline{True}(\alpha) = \begin{cases} True, & Indeterminacy < \alpha \\ \overline{True_{\alpha}}, & Indeterminacy \geq \alpha \end{cases} \tag{14}$$

$$\overline{True}_{\alpha}(x,y) = \left(\frac{1}{window \times window}\right) \sum_{m=i-window/2}^{i+window/2} \sum_{n=j-window/2}^{j+window/2} True(m,n) \tag{15}$$

$$\bar{F}alse(\alpha) = \begin{cases} False, & Indeterminacy < \alpha \\ \overline{False}, & Indeterminacy \geq \alpha \end{cases} \quad (16)$$

$$\bar{F}alse_{\alpha}(x, y) = \left(\frac{1}{window \times window}\right) \sum_{m=i-window/2}^{i+window/2} \sum_{n=j-window/2}^{j+window/2} False(m, n) \quad (17)$$

$$\overline{Indeterminacy}_{\alpha}(x, y) = \frac{\bar{\delta}_{True}(x, y) - \delta_{True_{min}}}{\delta_{True_{max}} - \delta_{True_{min}}} \quad (18)$$

$$\bar{\delta}_{T}(x, y) = abs(\bar{T}rue(x, y) - \overline{\overline{True}}(x, y)) \quad (19)$$

$$\bar{\bar{T}}rue(x, y) = \left(\frac{1}{window \times window}\right) \sum_{m=i-window/2}^{i+window/2} \sum_{n=j-window/2}^{j+window/2} \overline{True}(m, n) \quad (20)$$

where $\bar{\delta}_{True}$ is the AV between mean intensity and mean value.

Definition 5. Contrast intensification operator

In FS, the contrast intensification operator decreases the fuzziness of an FS A by increasing membership degree that is greater than 0.5, and reducing membership degree that is less than it [26]. In NS, the intensification is defined as part of β-enhancement operation by [27] that depending on the computed $\boldsymbol{\alpha}$ -mean operator. The intensification operator aims to enhance the truth and false degree based on the following rules:

$$\grave{T}rue_{intens}(\alpha) = \begin{cases} 2True^2, & \bar{T}rue(\alpha) \leq 0.5 \\ 1 - 2(1 - True(x, z))^2, & \overline{True}(\alpha) > 0.5 \end{cases} \quad (21)$$

$$Fa\grave{l}se_{intens}(\alpha) = \begin{cases} 2False^2, & \overline{False}(\alpha) \leq 0.5 \\ 1 - 2(1 - False(x, z))^2, & \overline{False}(\alpha) > 0.5 \end{cases} \quad (22)$$

Definition 6. $\boldsymbol{\beta}$-enhancement operation

$$\grave{P}(\beta) = P(Tr\grave{u}e(\beta), Indeter\grave{m}inacy(\beta), Fa\grave{l}se(\beta)) \quad (23)$$

$$Tr\grave{u}e(\beta) = \begin{cases} \bar{T}rue(\alpha), & \overline{Indeterminacy}_{\alpha}(x, y) < \beta \\ \grave{T}rue_{intens}(\alpha), & \overline{Indeterminacy}_{\alpha}(x, y) \geq \beta \end{cases} \quad (24)$$

$$\grave{F}(\beta) = \begin{cases} \bar{F}alse(\alpha), & Indeterminacy_{\alpha}(x, y) < \beta \\ \grave{T}_{intens}(\alpha), & \overline{Indeterminacy}_{\alpha}(x, y) \geq \beta \end{cases} \quad (25)$$

$$Indeter\grave{m}inacy_{\beta}(x, y) = \frac{\grave{\delta}_{True}(x, y) - \grave{\delta}_{True_{min}}}{\grave{\delta}_{True_{max}} - \grave{\delta}_{True_{min}}} \quad (26)$$

$$\grave{\delta}_{True}(x, y) = abs(Tr\grave{u}e(\beta) - \overline{Tr\grave{u}e}(x, y)) \quad (27)$$

$$\bar{\grave{T}}rue(x, y) = \left(\frac{1}{window \times window}\right) \sum_{m=i-window/2}^{i+window/2} \sum_{n=j-window/2}^{j+window/2} \grave{T}rue(m, n) \quad (28)$$

Since $\overline{Tr\grave{u}e}(x, y)$ is the AV between intensity and its LV after β-enhancement operation.

Definition 7. NS complement

The complement of NS is NS^c, where $True^c(\mathrm{x,y}) = False(\mathrm{x,y}), False^c(\mathrm{x,y}) = True(\mathrm{x,y}), Indeterminacy^c(\mathrm{x,y}) = 1 - Indeterminacy(\mathrm{x,y}), \mathrm{x,y} \in \mathcal{N}$.

Definition 8. Convert from NS domain

This process aims to transform form NS to crisp set [28]. The following equation is used to transform from NS domain to spatial domain

$$\widehat{\widehat{True}}(\mathcal{n}) = \bar{g}_{min} + (\bar{g}_{max} + \bar{g}_{min}.\widehat{True}(\mathcal{n})) \tag{29}$$

where $\widehat{True}(\mathcal{n})$ is the truth domain after enhancement.

4. Proposed method

In this section, we discuss two proposed frameworks BoneNet-NS1 and BoneNet-NS2 based on NS and different DL models.

4.1. BoneNet-NS1 framework

In this part, we describe the proposed BoneNet-NS1 framework which is based on NS input images to different DL models. The proposed BoneNet-NS1 framework is shown in Figure 2 and Algorithm 1. The main steps of the first proposed BoneNet-Ns1 framework can be summarized as:

Step 1: Convert RGB X-ray images to gray scale images

Each pixel in color image 24-bit is converted to gray scale 8-bit image in interval (0-255) where image size equals $W * H$.

Step 2: Compute LV of 8-bit image

The LV of a pixel in a $W * H$ gray picture may be determined by running a window across the image pixels. The window calculates the average value of nearby pixels for each pixel. In our study use a window measure 5 by 5.

Step 3: Compute the maximum and minimum values of LV.

Step 4: Compute True, Indeterminacy, and False in NS.

We calculate True, Indeterminacy, and False by Eqs. (4-8). Hence, every pixel within image will be denoted as: $\mathrm{P(a,b) = P(True(a,b), Indeterminancy(a,b), False(a,b))}$.

Step 5: Apply classification model

The NS image is an input to the DL model such as Xception, ResNet152V2, DenseNet121, and customized CNN to evaluate their performance using the NS image. The DL learning model classified the bone X-ray images as fractured or not fractured. The customized CNN is implemented as demonstrated in Table 2.

Table 2 Customized CNN architecture

Layer name	Filters	Kernel size	Activation	Pool size	Output size
Conv2d	32	(3,3)	Relu	-	222 x 222
BatchNormalization	-	-	-	-	222 x 222
Max pooling 2d	-	-	-	(2,2)	111 x 111
Conv2d	64	(3,3)	Relu	-	109 x 109
BatchNormalization	-	-	-	-	109 x 109
Max pooling 2d	-	-	-	(2,2)	54 x 54
Dropout	Dropout percentage is 0.3				54 x 54
Conv2d	128	(3,3)	Relu	-	52 x 52
BatchNormalization	-	-	-	-	52 x 52
Max pooling 2d	-	-	-	(2,2)	26 x 26
Dropout	Dropout percentage is 0.3				54 x 54
Flatten	-				86528
Dense	Dense (256)		Relu	-	256
Dropout	Dropout percentage is 0.3				256
Dense	Dense (128)		Relu	-	128
Dropout	Dropout percentage is 0.3				128
Dense	Desne (1)		sigmoid	-	1

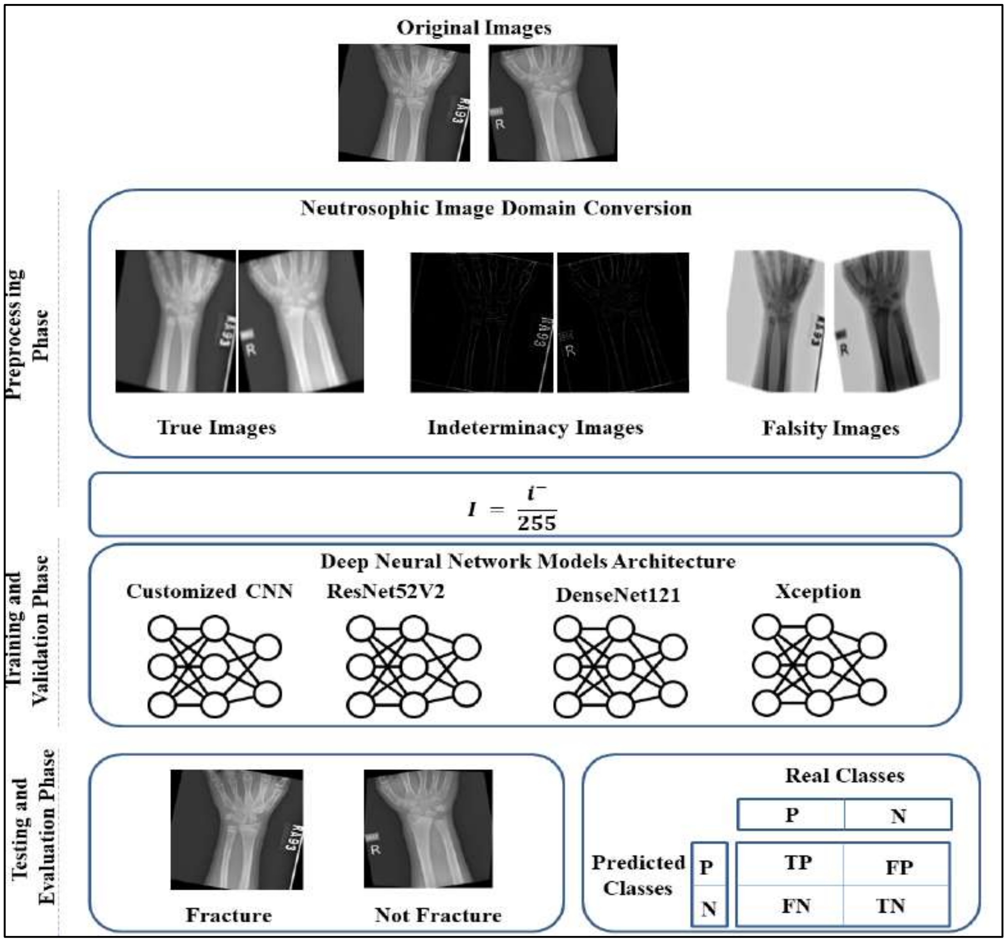

Figure 2 The BoneNet-NS1 general framework

Algorithm 1 BoneNet-NS1 for bone fracture classification approach

Input: Gray image with intensities in interval from 0 to 255**.**

For each pixels in image **do**

A 5×5 filter, to obtain the LV.

Obtain the min and max of LV.

Represent each pixel into NS image using Eqs. 4-8.

Classify the NS images using DL model**.**

End

Output: return class

4.2. BoneNet-NS2 framework

In this part, we describe the proposed BoneNet-NS2 framework which is based on NS enhancement operations on X-ray bone images and DL models. The steps from 1 to 4 in BoneNet-NS1 framework are similar in BoneNet-NS2 framework first four steps. The DL model input in the second framework is gray scale image that previously enhanced under NS domain. The proposed BoneNet-NS2 framework is shown in Figure 3 and Algorithm 2. The main steps of BoneNet-NS2 framework can be summarized as:

Step 1: Convert RGB X-ray images to gray scale images

Each pixel in color image 24-bit is converted to gray scale 8-bit image in interval (0-255) where image size equals $W * H$.

Step 2: Compute LV of 8-bit image

The LV of a pixel in a $W * H$ gray picture may be determined by running a window across the image pixels. The window calculates the average value of nearby pixels for each pixel. In our study we use window measure 5 by 5.

Step 3: Compute the maximum and minimum values of LV.

Step 4: Compute True, Indeterminacy, and False in NS.

We calculate True, Indeterminacy, and False by Eqs. (4-8). Hence, every pixel within image will be denoted as: *P(a, b) = P(True(a, b), Indeterminancy(a, b), False(a, b))*.

Step 5: Perform enhancement operation

The enhancement operation aims to minimize the indeterminacy data and enhances the truth data. This operation is obtained by α-mean, intensification, and β-enhancement operators. The α-mean operation and β-enhancement operation, are used to minimize the indeterminacy image. The mean value between neighbors can be defined by α-mean operation. The α and β parameters can represented as follows [29]

$$\alpha = \alpha_{min} + \frac{(\alpha_{max} - \alpha_{min})(EntropyI - Entropy_{min})}{(Entropy_{max} - Entropy_{min})} \tag{39}$$

$$\beta = 1 - \alpha \tag{40}$$

$$EntropyI = \sum_{i=1}^{W} \sum_{j=1}^{H} pixel(x, y) \log_2 pixel(x, y) \tag{41}$$

$$EN_{max} = -\log_2 \frac{1}{hw} \tag{42}$$

Since the W and H are the width and height of image. Our study uses a modified approach to compute α and β parameters, enhancing the results under the NS domain using Equations (39) to (42). Then, $\alpha - mean$, intensification operation, and $\beta - enhancment$ operation is calculated on the truth image based on Eqs. (13-28). The Entropy in Eqs. (9-12) calculates the alteration of the local pixels. The α-mean operation provides high entropy of indeterminacy image and uniform distribution, while the β-enhancement operation enhances the true image. This procedure improves the sensitivity of the indeterminacy image to local pixels. The NS enhancement operation is demonstrated in Figure 4.

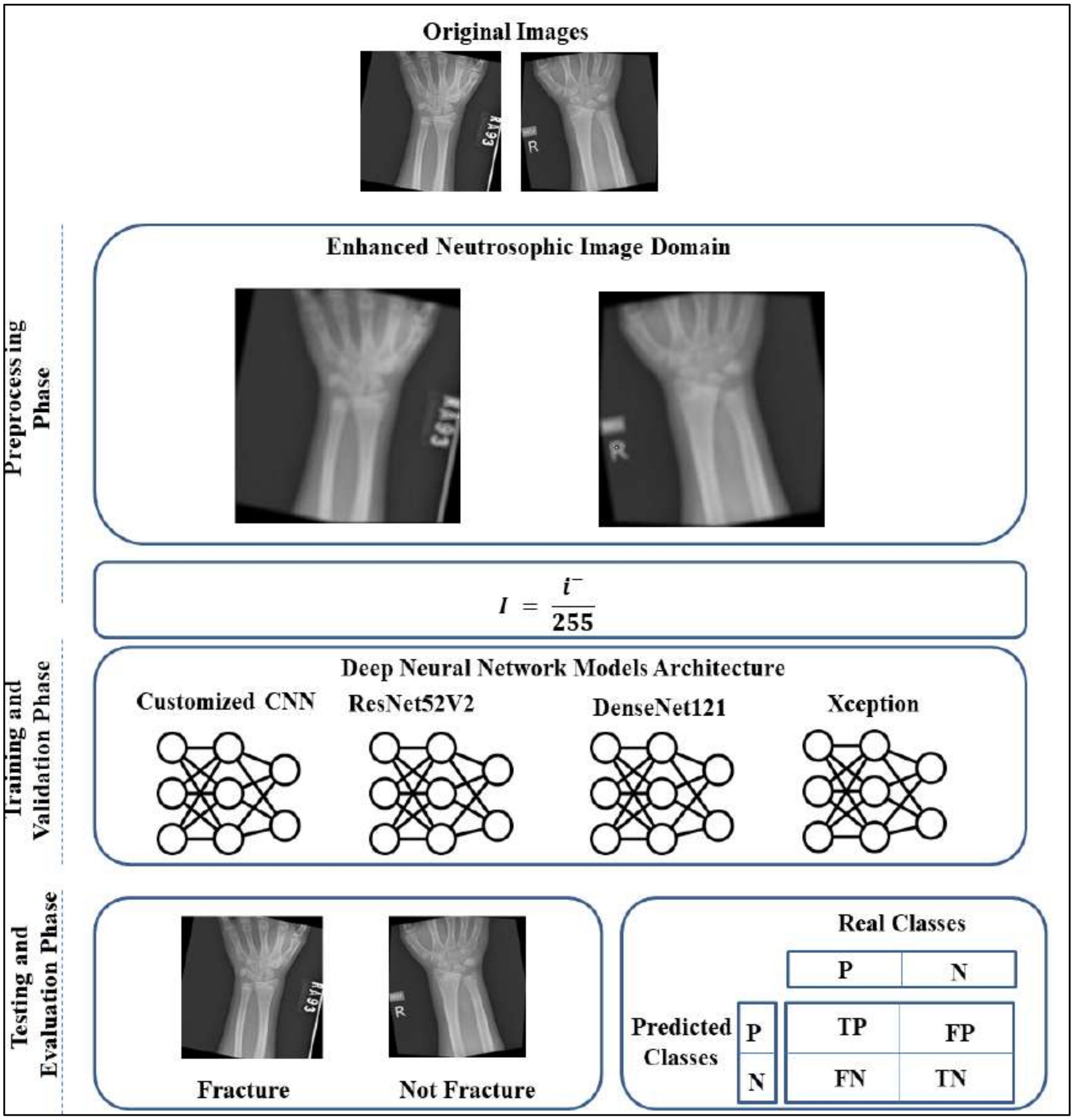

Figure 3 The BoneNet-NS2 general framework.

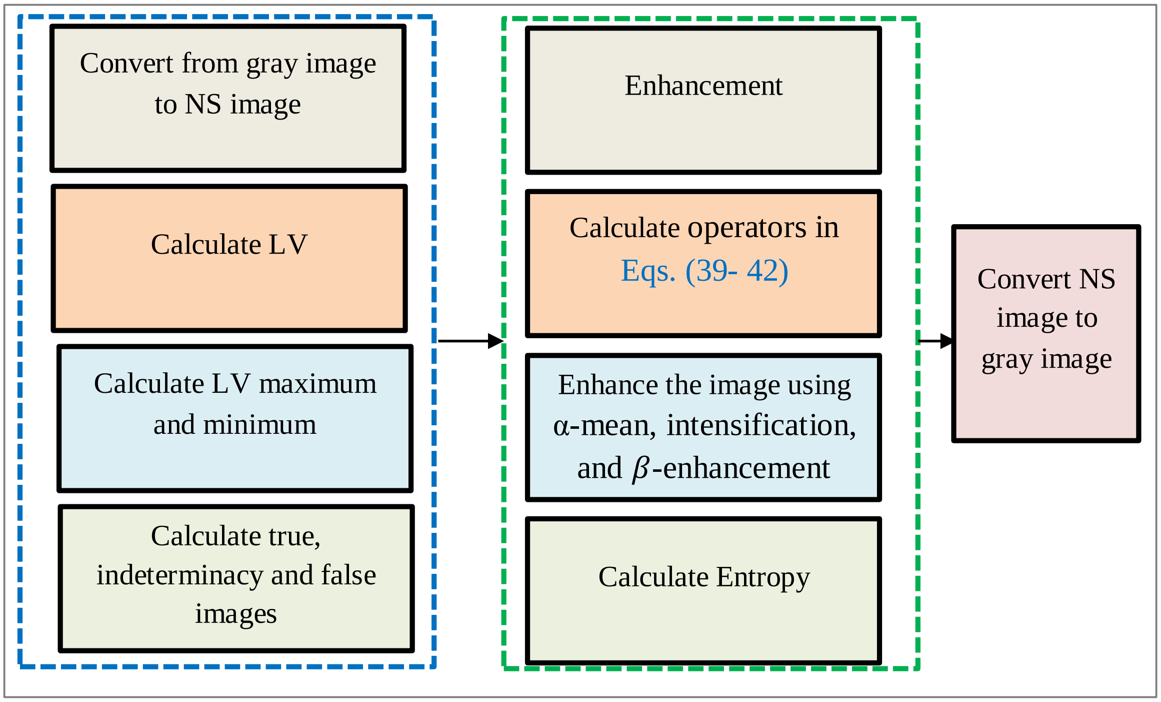

Figure 4 NS enhancement operations

Algorithm 2 BoneNet-NS2 for bone fracture classification approach

Input: Gray image with intensities in interval from 0 to 255.

For each pixels in image **do**

A 5×5 filter, to obtain the LV.
Obtain the min and max of LV.
Represent each pixel into NS image using Eqs. (4-8).
Calculate α, β parameters using Eqs. (39-42).
Obtain α-mean operation using Eqs. (13-20).
Obtain intensification operation using Eqs. (21-22).
Obtain β-enhancement operation Eqs. (23-28).
Calculate entropy to enhance True image Eqs. (9-12).
Convert NS image to gray image Eq. (29)
Classify the enhanced images using DL model.

End

Output: return class.

5. Experimental results

This section includes: the bone X-ray image dataset settings, evaluation metrics, implementation settings, visualization of proposed approach, statistical analysis related to bone X-ray image classification are illustrated.

5.1. Dataset settings

Our proposed is evaluated using 4924 bone X-ray images from Kaggle dataset [30]. The bone fractured dataset was adjusted to a resolution of 224 x 244 pixels divided into training, validation, and testing data. The data is classified into two classes (fracture and non-fractured). The bone X-ray dataset description is summarized in Table 3 and Figure 5.

Table 3 Bone X-ray dataset description.

	Fractured	Non-fractured	Total Classes
Train	2097	2020	4117
Test	200	201	401
Validation	169	237	406
Total	2466	2458	**4924**

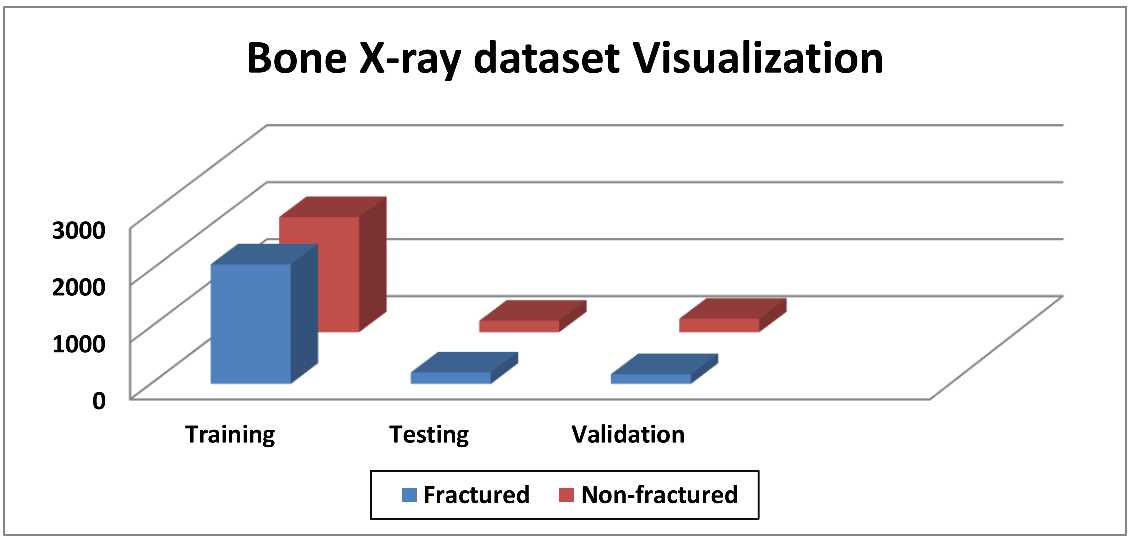

Figure 5 Bone X-ray dataset visualization.

5.2. Evaluation metrics

Our proposed work was evaluated using binary cross entropy/log loss, accuracy, precision, recall, F1-score, and AUC.

- **Binary cross entropy/log loss** is a loss function used to evaluate the change between predicted binary outcomes and actual binary labels which can be denoted as follows [31]:

$$-\frac{1}{N}\sum_{i=1}^{N} y_i \cdot \log(p(y_i)) + (1 - y_i) \cdot \log(1 - p(y_i)) \tag{43}$$

- To displaying a confusion matrix of proposed work, the following metrics can be computed:

$$Accuracy = \frac{TP + TN}{(TP + FP + TN + FN)} \tag{44}$$

$$Precision = \frac{TP}{(TP+FP)}) \tag{45}$$

$$Recall = \frac{TP}{(TP+FN)} \tag{46}$$

$$F1 - score = 2 * \frac{Precision \cdot Recall}{(Precision + Recal)} \tag{47}$$

Where TP, FN, TN, and FP represent the number of true positive, the number of false negative, the number of true negative, and the number false positive, respectively

- **Area under the curve (AUC)** is a single measure that expresses how well a binary classification model performs overall in differentiating between positive and negative examples [32].

$$ROC \quad -AUC = \int_0^1 TPR(FPR)\mathrm{d}FPR = \int_0^1 TPR(FPR^{-1}(x))\mathrm{d}x \tag{48}$$

Where TPR , FPR represent True Positive Rate and False Negative Rate

5.3. Implementation settings

Table 4 describes a complete detail of our implementations in consideration of parameters used training DL models.

Table 4 Implementation settings

Frameworks	Python using the Kaggle platform and keras API
Optimizer	Adam
Epochs for customized CNN	20
Epochs for other DL models	10
Batch size	32

5.4. Visualization analysis

In this section, we introduce the visual analysis for our approach. We support our experiments on radiological bone images for NS algorithm Figures 6. Figure 6 shows the two different inputs for two proposed frameworks. Figures 6 (b), (c), and (D) show the NS image, which is the input to the BoneNet-NS1. Figure 6 (e) shows the final converted gray image, which is the input to BoneNet-NS2 after performing some enhancement operations under the NS environment.

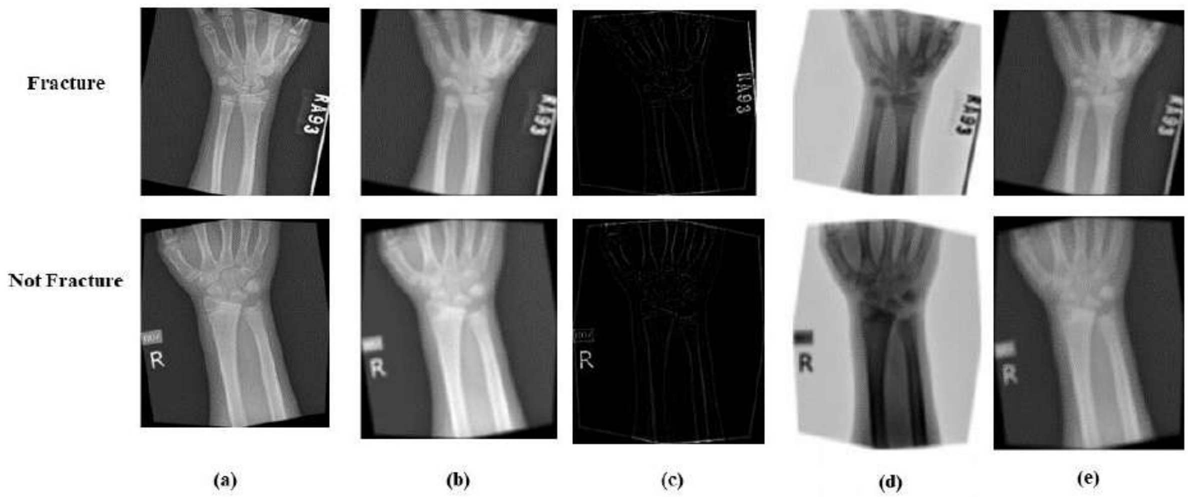

Figure 6 bone dataset under NS domain (a) original images, (b) True image, (c) Indeterminacy image, (d) Falsity image, and (e) Enhanced grayscale image.

5.5. Statistical analysis

In this section, we discuss the efficiency of our approach to bone X-ray fracture classification using the NS and DL models. We introduce two frameworks for NS and DL integration. The first framework (BoneNet-NS1) uses an NS image as an input to the DL model. The second framework (BoneNet-NS2) uses a gray image that was previously enhanced under NS domain using $\alpha - mean$ and $\beta - enhancment$ operations. Our approach was evaluated using four different DL models such as Xception, ResNet152V2, DenseNet121, and customized CNN. Table 5 and Table 8 show results of accuracy, log loss, precision, recall, F1-score, and AUC. The table shows superior results in terms of accuracy for the Xception model.

The first framework (BoneNet-NS1) was applied to Xception, ResNet152V2, DenseNet, and customized CNN models, and their results are summarized in Table 6 and Table 9. The results show superior results in True and indeterminacy domains for ResNet152V2, DenseNet121, and customized CNN. But in the false domain, the Xception and customized CNN show lower results than the results in Table 5.

The second framework (BoneNet-NS2) was applied to Xception, ResNet152V2, DenseNet, and customized CNN models, and their results are summarized in Table 7 and Table 10. The Bone-Net-NS2 shows superior results for all models than Table 5 and Table 6. ResNet52V2 shows the highest results using (BoneNet-NS2) in terms of accuracy, log loss, precision, recall, F1-score, and AUC with 99.7 %, 0.006, 99.7%, 99.7%, 99.7%, and 99.7, respectively.

Table 5 Evaluation of DL model on bone X-ray dataset before using NS

Model	Accuracy	log loss	Precision	Recall	F1-score	AUC
Xception	**0.994**	0.014	0.995	0.995	0.994	0.995
ResNet152V2	0.989	0.034	0.990	0.989	0.989	0.989
DenseNet121	0.962	0.089	0.962	0.962	0.962	0.962
Customized CNN	0.939	0.324	0.942	0.939	0.939	0.939

Table 6 Evaluation of DL model on bone X-ray dataset using BoneNet-NS1

True domain						
Model	**Accuracy**	**log loss**	**Precision**	**Recall**	**F1-score**	**AUC**
Xception	0.994	0.014	0.995	0.995	0.994	0.995
ResNet152V2	**0.994**	**0.013**	**0.995**	**0.995**	**0.994**	**0.995**
DenseNet121	**0.992**	**0.024**	**0.992**	**0.992**	**0.992**	**0.992**
Customized CNN	**0.944**	**0.243**	**0.946**	**0.944**	**0.944**	**0.944**
Indeterminacy domain						
Xception	0.974	0.052	0.975	0.974	0.974	0.974
ResNet152V2	**0.992**	**0.018**	**0.992**	**0.992**	**0.992**	**0.992**
DenseNet121	**0.984**	**0.050**	**0.985**	**0.984**	**0.984**	**0.984**
Customized CNN	**0.969**	**1.325**	**0.971**	**0.970**	**0.969**	**0.97**
False domain						
Xception	0.994	0.016	0.995	0.995	0.994	0.995
ResNet152V2	**0.997**	**0.005**	**0.997**	**0.997**	**0.997**	**0.997**
DenseNet121	**0.987**	**0.033**	**0.987**	**0.987**	**0.987**	**0.987**
Customized CNN	0.796	1.579	0.827	0.797	0.792	0.797

Table 7 Evaluation of DL model on bone X-ray dataset using BoneNet-NS2

Model	Accuracy	log loss	Precision	Recall	F1-score	AUC
Xception	**0.997**	**0.014**	**0.997**	**0.997**	**0.997**	**0.997**
ResNet52V2	**0.997**	**0.006**	**0.997**	**0.997**	**0.997**	**0.997**
DenseNet121	**0.972**	**0.098**	**0.972**	**0.972**	**0.972**	**0.972**
Customized CNN	**0.962**	**0.260**	**0.962**	**0.962**	**0.962**	**0.962**

Table 8 Confusion matrix and ROC of DL model on bone X-ray dataset before using NS

<table>
<tr><th>Model</th><th>Confusion Matrix</th><th>Roc Curve</th></tr>
<tr><td>Xception</td><td>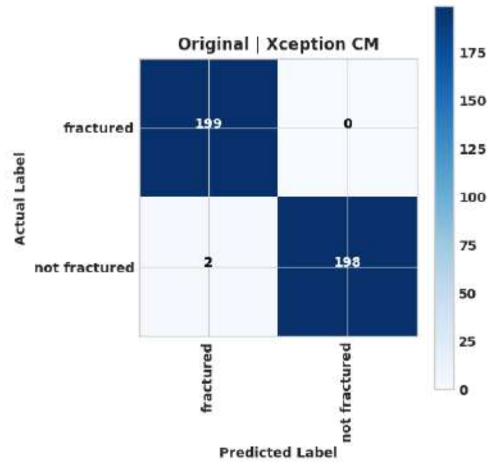
</td><td>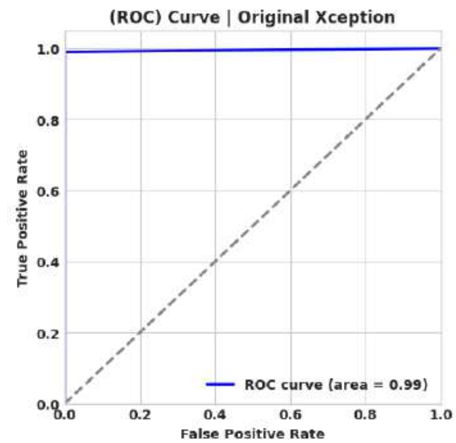
</td></tr>
<tr><td>ResNet52V2</td><td>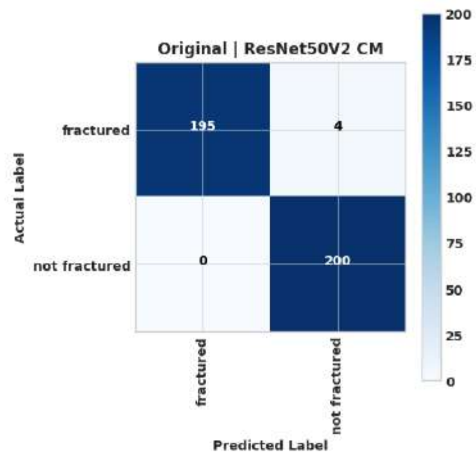
</td><td>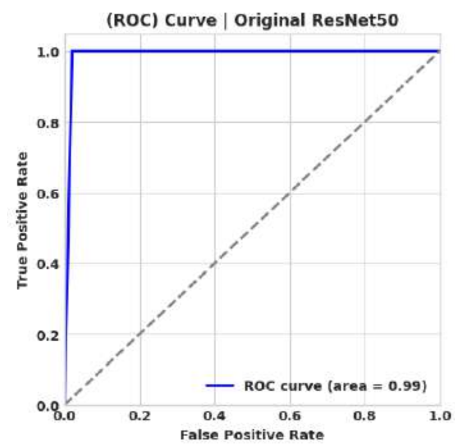
</td></tr>
<tr><td>DenseNet121</td><td>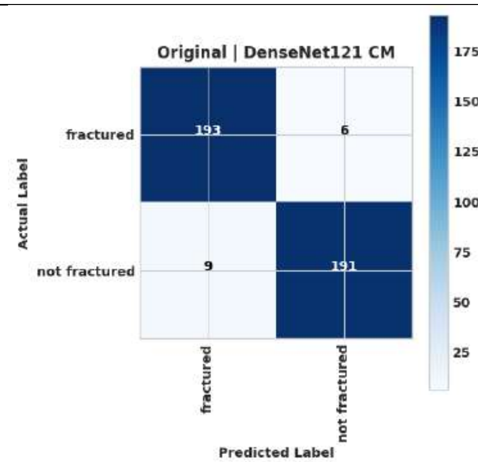
</td><td>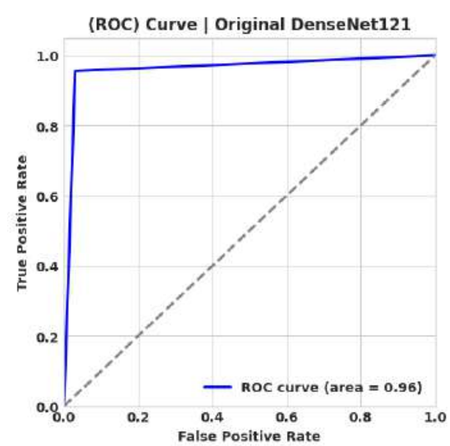
</td></tr>
</table>

Customized CNN	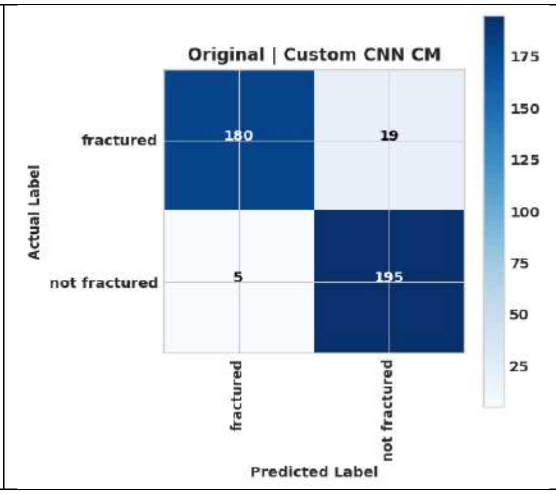	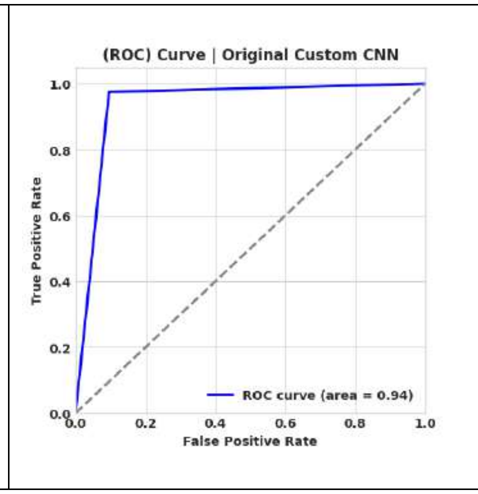

Table 9 Confusion matrix and ROC of DL model on bone X-ray dataset After using BoneNet-NS1

T Dataset		
Model	**Confusion Matrix**	**Roc Curve**
Xception	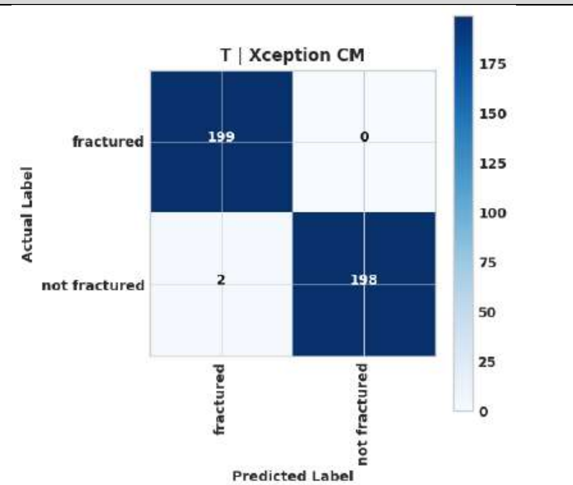	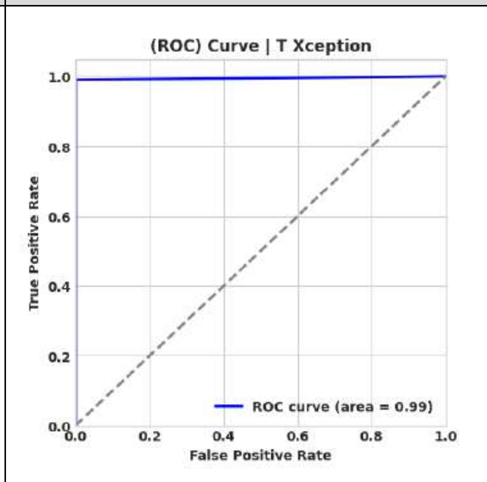
ResNet52V2	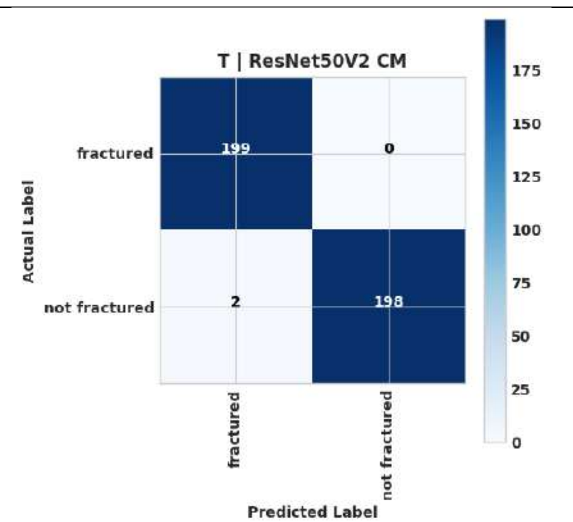	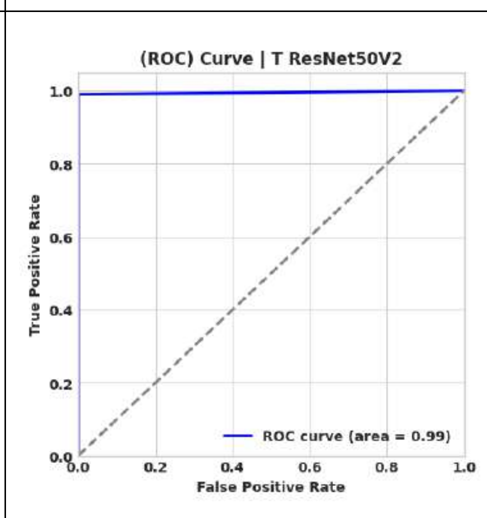

<table>
<tr><td>DenseNet121</td><td>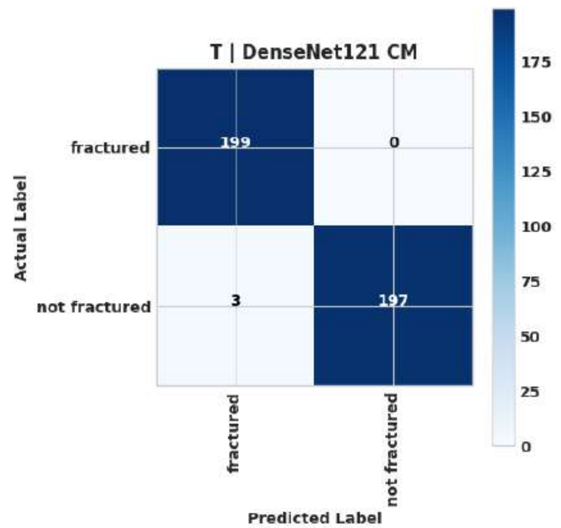
</td><td>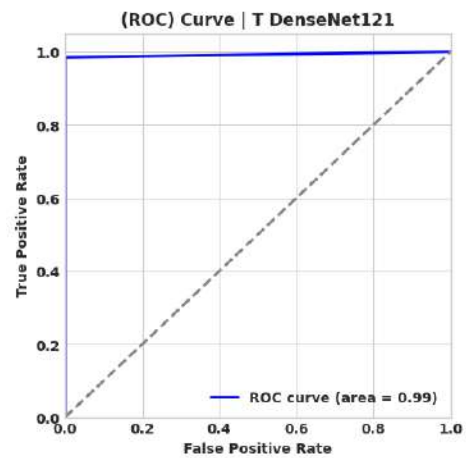
</td></tr>
<tr><td>Custom CNN</td><td>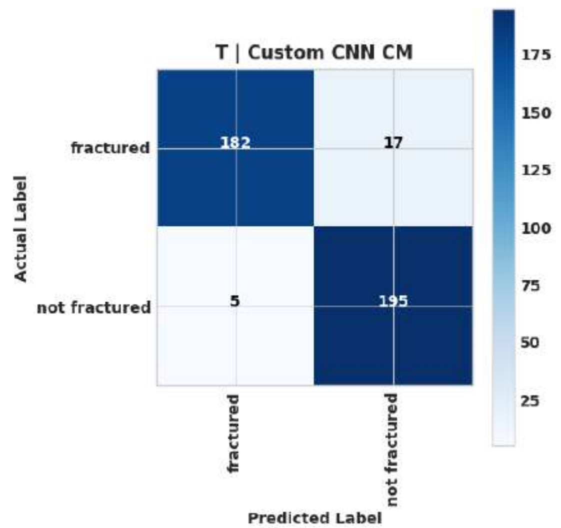
</td><td>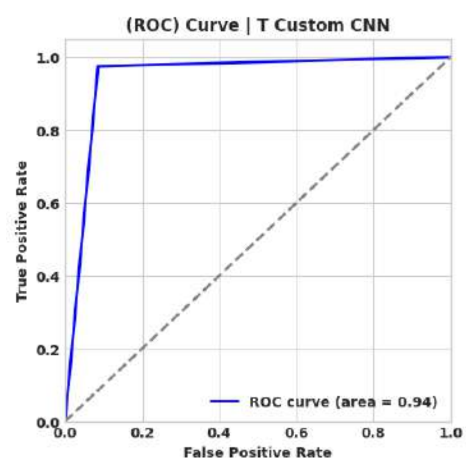
</td></tr>
<tr><td colspan="3">I Dataset</td></tr>
<tr><td>Xception</td><td>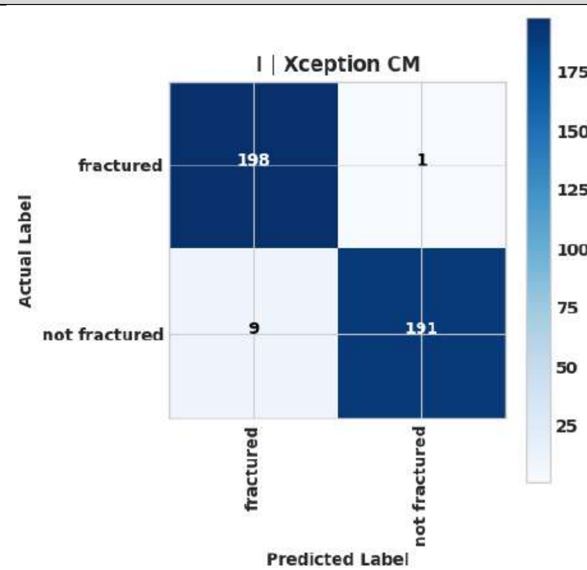
</td><td>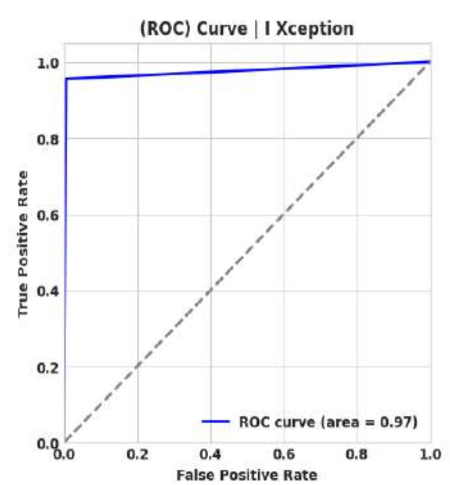
</td></tr>
</table>

ResNet52V2	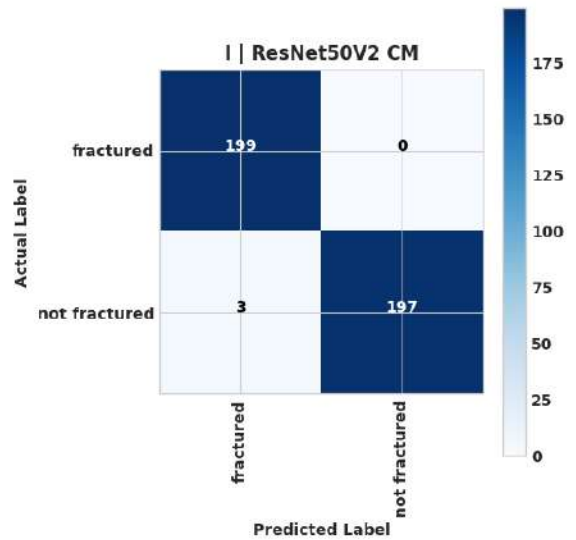	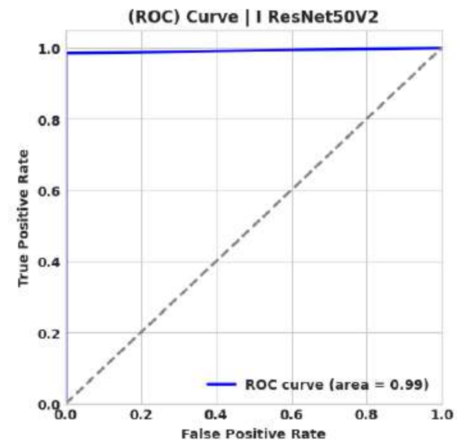
DenseNet121	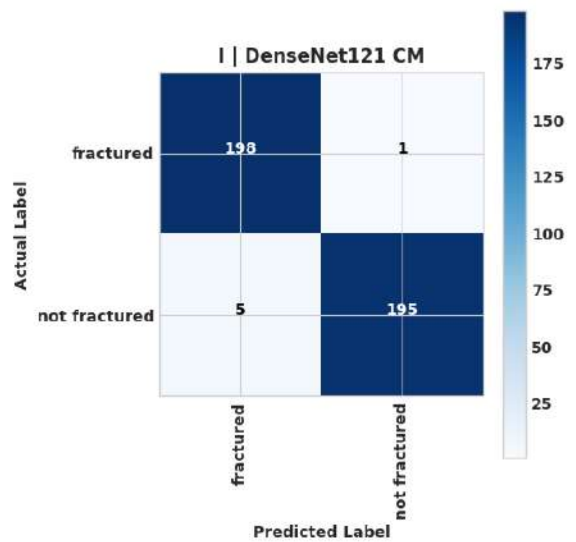	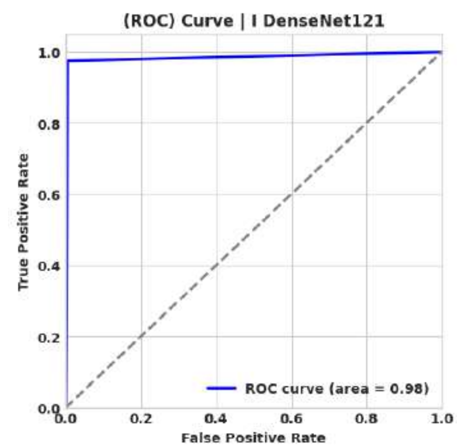
Custom CNN	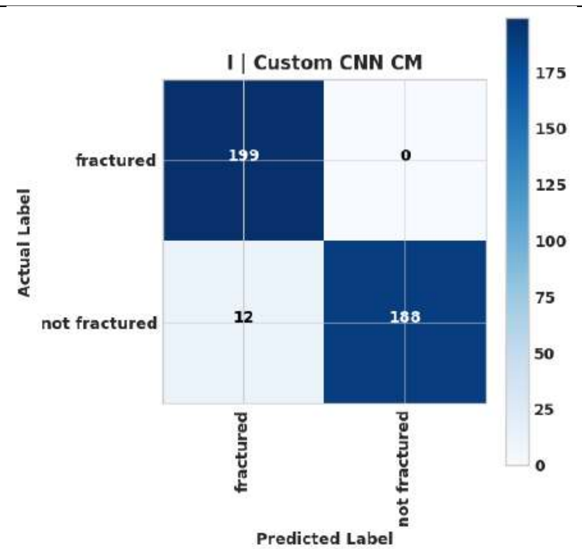	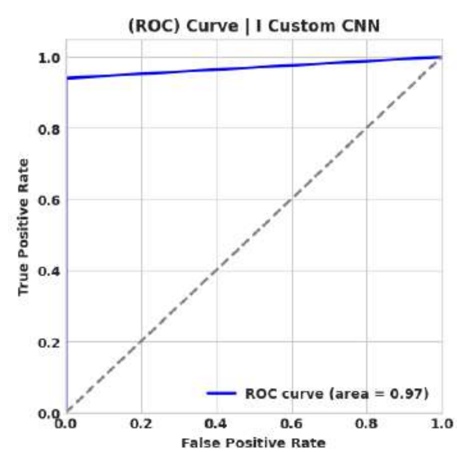
F Dataset		

Xception	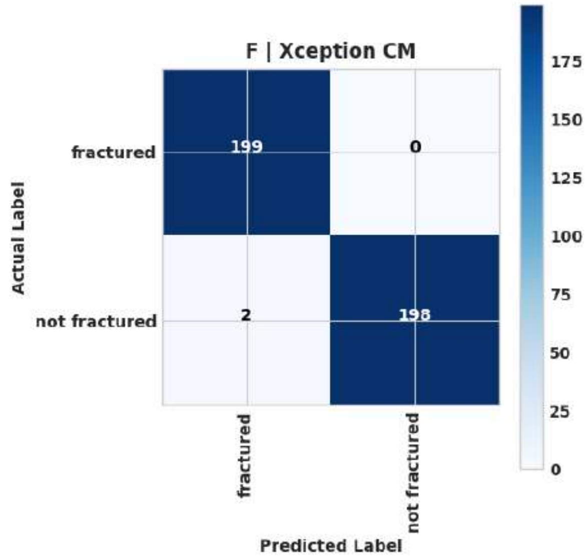	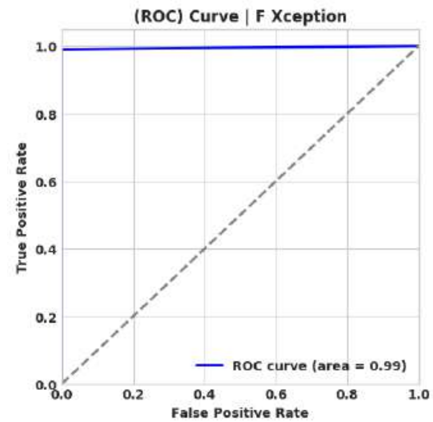
ResNet52V2	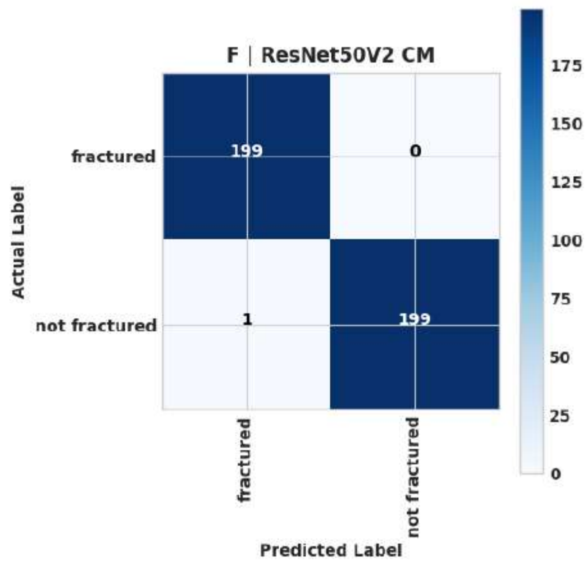	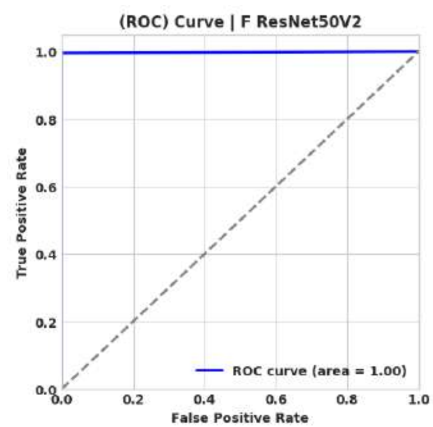

<table>
<tr><td>DenseNet121</td><td>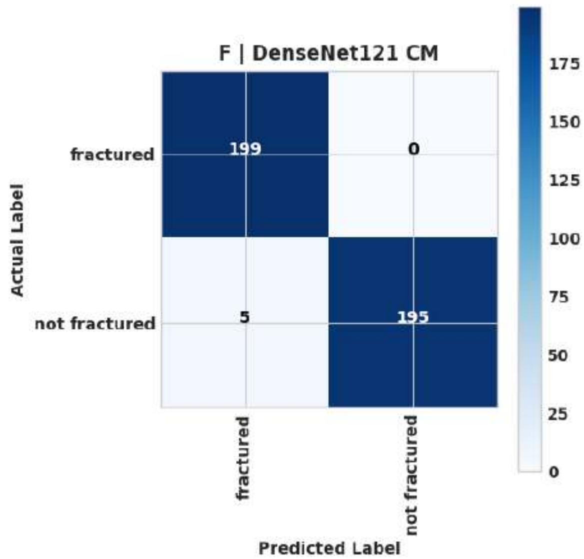</td><td>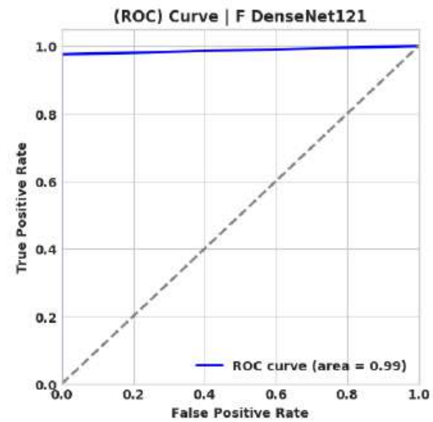</td></tr>
<tr><td>Custom CNN</td><td>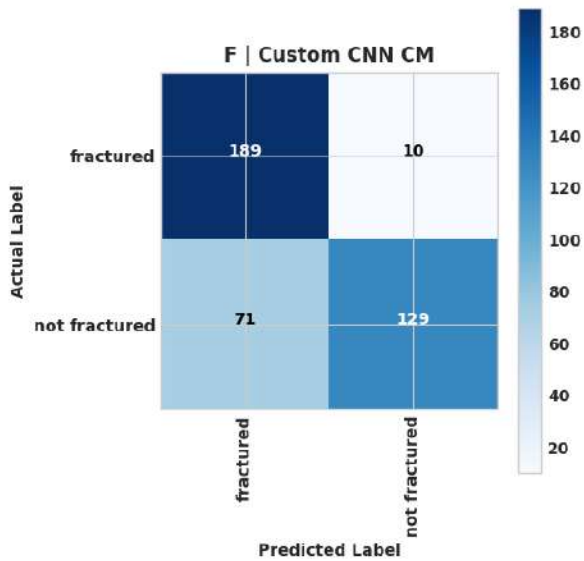</td><td>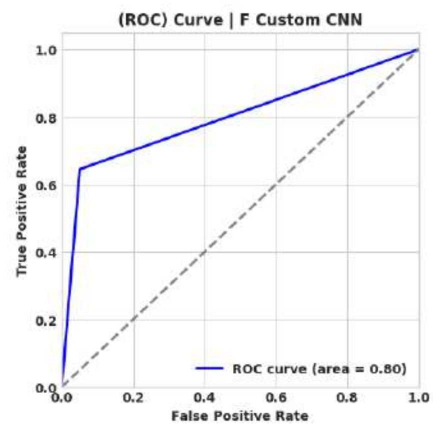</td></tr>
</table>

Table 10 Confusion matrix and ROC of DL model on bone X-ray dataset After using BoneNet-NS2

<table>
<tr><th>Model</th><th>Confusion Matrix</th><th>Roc Curve</th></tr>
<tr><td>Xception</td><td>
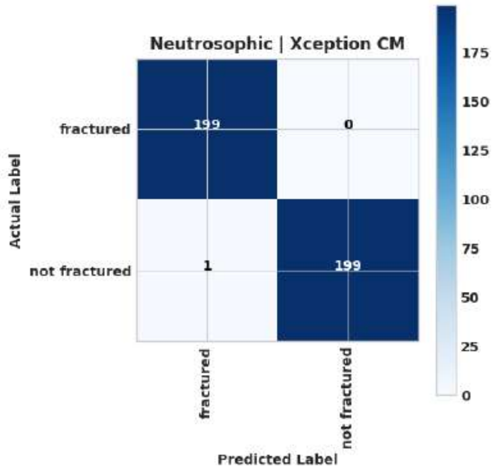

</td><td>
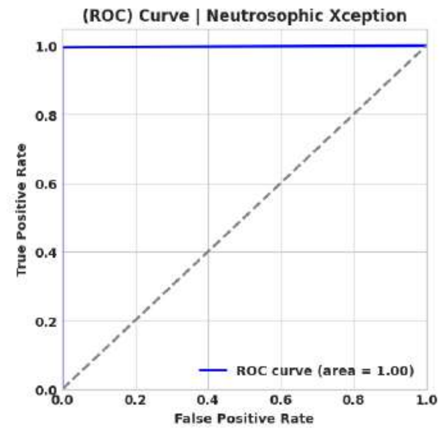

</td></tr>
<tr><td>ResNet52V2</td><td>
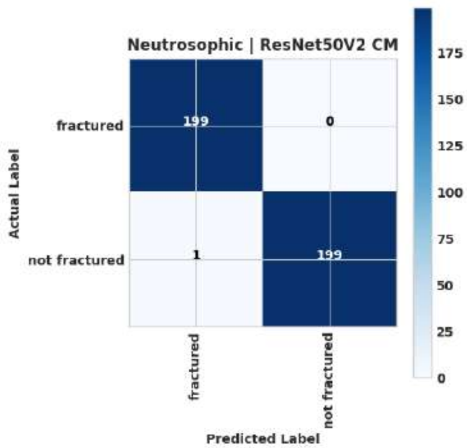

</td><td>
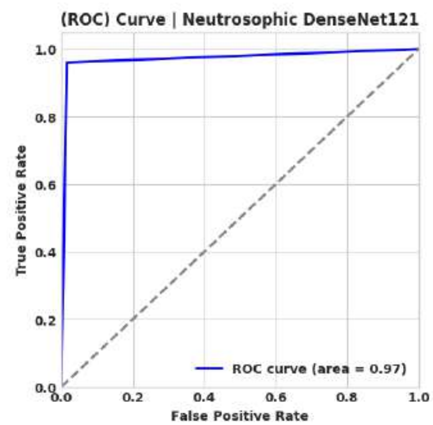

</td></tr>
<tr><td>DenseNet121</td><td>
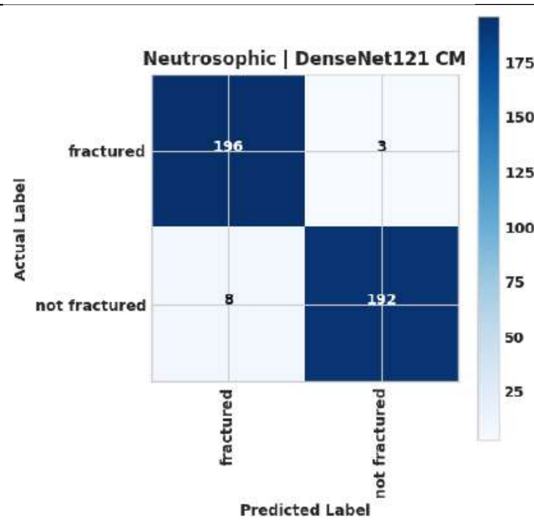

</td><td>
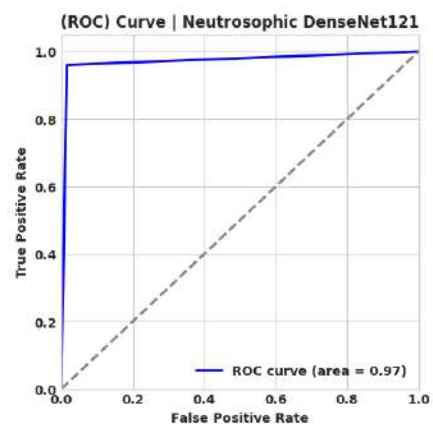

</td></tr>
</table>

Custom CNN	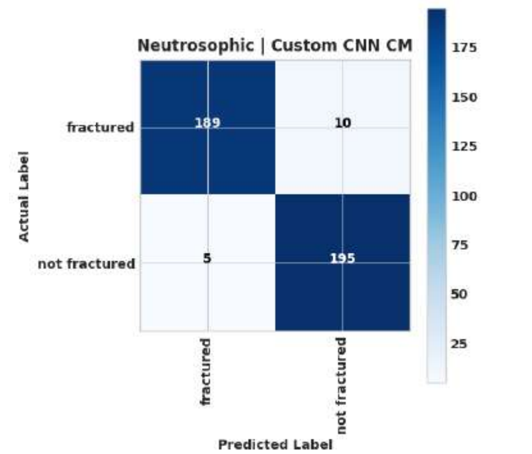	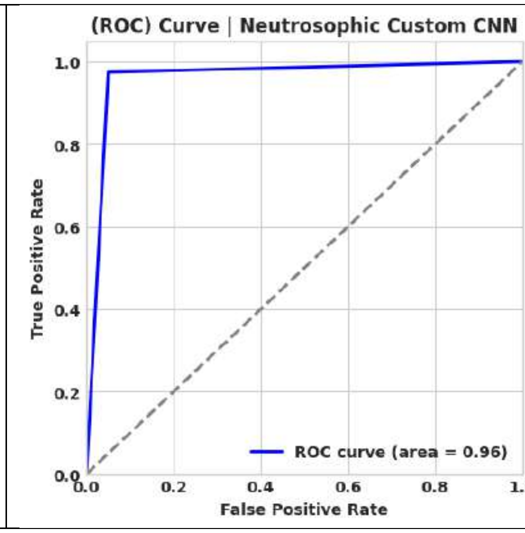

6. Managerial implementation

Sustainable development indicators contribute to assessing the progress of countries and institutions in achieving sustainable development goals. These indicators revolve around the recommendations of the Twenty-First Century Agenda set by the United Nations, which include appropriate health care for all members of society, especially remote and rural areas, to control endemic and epidemic diseases resulting from environmental pollution. We introduce an automatic approach for bone fracture identification using X-ray images based on DL and NS techniques. The proposed approach can reduce the increasing pressure on healthcare infrastructure.

7. Conclusion

The NS environment classification approach depends on only three degrees of membership. Using NS and DL for classification tasks can provide more ability to deal with uncertainty and increase the performance and accuracy of classification tasks. The main challenge of this study is that bone radiological image contains aleatoric uncertainty which leads to bad contrast and inconsistent boundaries. This affects the performance of bone fractured classification and identification. In our study, we introduce two frameworks: BoneNet-NS1 and BoneNet-NS2 for bone fractured classification using X-ray images. The proposed framework is based on different DL models and NS to handle uncertainty data in images. The second framework shows superior results during using -mean and enhancement operations under the NS domain and input this enhanced gray image to DL models. The proposed framework was evaluated on bone fracture X-ray dataset on 4924 images. The second framework shows superior results with most DL models. The higher results were shown in the proposed (BoneNet-NS2) on ResNet52V2 in terms of accuracy, log loss, precision, recall, F1-score, and AUC with 99.7 %, 0.006, 99.7%, 99.7%, 99.7%, and 99.7, respectively.

References

1. Cha, Y., et al., *Artificial intelligence and machine learning on diagnosis and classification of hip fracture: systematic review.* Journal of Orthopaedic Surgery and Research, 2022. **17**(1): p. 520.
2. Zou, K., et al., *A review of uncertainty estimation and its application in medical imaging.* Meta-Radiology, 2023: p. 100003.
3. Sambyal, A.S., N.C. Krishnan, and D.R. Bathula. *Towards reducing aleatoric uncertainty for medical imaging tasks*. in *2022 IEEE 19th International Symposium on Biomedical Imaging (ISBI)*. 2022. IEEE.
4. Deheyab, A.O.A., et al. *An overview of challenges in medical image processing*. in *Proceedings of the 6th International Conference on Future Networks & Distributed Systems*. 2022.
5. Zadeh, L.A., *Fuzzy sets as a basis for a theory of possibility.* Fuzzy sets and systems, 1978. **1**(1): p. 3-28.
6. Vasilakakis, M., et al. *Bone fracture identification in x-ray images using fuzzy wavelet features*. in *2019 IEEE 19th International Conference on Bioinformatics and Bioengineering (BIBE)*. 2019. IEEE.
7. Singh, C., et al., *A novel approach for brain MRI segmentation and image restoration under intensity inhomogeneity and noisy conditions.* Biomedical Signal Processing and Control, 2024. **87**: p. 105348.
8. Smarandache, F., et al., *Introduction to neutrosophy and neutrosophic environment*, in *Neutrosophic Set in Medical Image Analysis*. 2019, Elsevier. p. 3-29.
9. Mohan, J., V. Krishnaveni, and Y. Guo, *A new neutrosophic approach of Wiener filtering for MRI denoising.* Measurement Science Review, 2013. **13**(4): p. 177-186.
10. Can, Z., S. Isik, and Y. Anagun, *CVApool: using null-space of CNN weights for the tooth disease classification.* Neural Computing and Applications, 2024.
11. Wang, J., et al., *A Hybrid Deep Learning-Based Framework for Chip Packaging Fault Diagnostics in X-Ray Images.* IEEE Transactions on Industrial Informatics, 2024: p. 1-11.
12. Khalifa, N.E.M., et al., *A study of the neutrosophic set significance on deep transfer learning models: An experimental case on a limited covid-19 chest x-ray dataset.* Cognitive Computation, 2021: p. 1-10.
13. Hu, K., et al., *Colorectal polyp region extraction using saliency detection network with neutrosophic enhancement.* Computers in Biology and Medicine, 2022. **147**: p. 105760.
14. Cai, G., et al., *14 - Neutrosophic set-based deep learning in mammogram analysis*, in *Neutrosophic Set in Medical Image Analysis*, Y. Guo and A.S. Ashour, Editors. 2019, Academic Press. p. 287-310.
15. Yasser, I., et al., *A hybrid automated intelligent COVID-19 classification system based on neutrosophic logic and machine learning techniques using chest X-Ray images.* Advances in Data Science and Intelligent Data Communication Technologies for COVID-19: Innovative Solutions Against COVID-19, 2022: p. 119-137.
16. Yasser, I., et al., *COVID-X: novel health-fog framework based on neutrosophic classifier for confrontation covid-19.* Neutrosophic Sets and Systems, 2020. **35**: p. 1-21.
17. Guo, Y. and A.S. Ashour, *13 - Neutrosophic multiple deep convolutional neural network for skin dermoscopic image classification*, in *Neutrosophic Set in Medical Image Analysis*, Y. Guo and A.S. Ashour, Editors. 2019, Academic Press. p. 269-285.
18. Özyurt, F., et al., *Brain tumor detection based on Convolutional Neural Network with neutrosophic expert maximum fuzzy sure entropy.* Measurement, 2019. **147**: p. 106830.
19. Ghanbari Talouki, A., A. Koochari, and S. Ahmad Edalatpanah, *Image completion based on segmentation using neutrosophic sets.* Expert Systems with Applications, 2024. **238**: p. 121769.
20. Guo, Y., A.I. Shahin, and H. Garg, *An indeterminacy fusion of encoder-decoder network based on neutrosophic set for white blood cells segmentation.* Expert Systems with Applications, 2024. **246**: p. 123156.
21. Smarandache, F., *A unifying field in Logics: Neutrosophic Logic*, in *Philosophy*. 1999, American Research Press. p. 1-141.
22. Zhang, M., L. Zhang, and H.-D. Cheng, *A neutrosophic approach to image segmentation based on watershed method.* Signal Processing, 2010. **90**(5): p. 1510-1517.
23. Wang, H., Y.-Q. Zhang, and R. Sunderraman. *Truth-value based interval neutrosophic sets*. in *2005 IEEE International Conference on Granular Computing*. 2005. IEEE.
24. Singh, P., *A type-2 neutrosophic-entropy-fusion based multiple thresholding method for the brain tumor tissue structures segmentation.* Applied Soft Computing, 2021. **103**: p. 107119.
25. Guo, Y. and H.D. Cheng, *New neutrosophic approach to image segmentation.* Pattern Recognition, 2009. **42**(5): p. 587-595.
26. Rangasamy, P., et al., *Role of fuzzy and intuitionistic fuzzy contrast intensification operators in enhancing images.* Notes Intuitionistic Fuzzy Sets, 2008. **14**(2): p. 59-66.
27. Guo, Y. and H.-D. Cheng, *New neutrosophic approach to image segmentation.* Pattern Recognition, 2009. **42**(5): p. 587-595.
28. Singh, P. and K. Rabadiya. *Information classification, visualization and decision-making: A neutrosophic set theory based approach*. in *2018 IEEE International Conference on Systems, Man, and Cybernetics (SMC)*. 2018. IEEE.
29. Sengur, A. and Y. Guo, *Color texture image segmentation based on neutrosophic set and wavelet transformation.* Computer Vision and Image Understanding, 2011. **115**(8): p. 1134-1144.
30. Kong, X., et al., *Multi-step short-term solar radiation prediction based on empirical mode decomposition and gated recurrent unit optimized via an attention mechanism.* Energy, 2023. **282**: p. 128825.
31. Hurtik, P., et al., *Binary cross-entropy with dynamical clipping.* Neural Computing and Applications, 2022. **34**(14): p. 12029-12041.
32. Bradley, A.P., *The use of the area under the ROC curve in the evaluation of machine learning algorithms.* Pattern recognition, 1997. **30**(7): p. 1145-1159.

Received: Mar 1, 2024. Accepted: May 31, 2024